600 km s^{-1} could escape detection; this is unlikely, as 600 km s^{-1} is greater than the escape velocity. Consequently, neither J-level population ($J = 2$ is not detected) nor Doppler shift can explain the discrepancy. If the H_2 seen in the infrared were located in the disk, it would have been detected in our FUSE observation.

A solution to this problem is to consider that H_2 is not distributed widely throughout the disk. If the ISO detection is confirmed by further observations, we suggest that the H_2 could be confined into individual clouds, none of which intersected the small volume of the β Pic line of sight at the time of our FUSE observations. Such H_2 clouds would easily escape detection in absorption, but would be seen in emission. The nature of these clouds remains unclear; however, we speculate that they might be remnants of gaseous planet embryos which captured a significant amount of protoplanetary material before its recent dissipation. The stability, number and density of these putative clouds need to be analysed. Given that 0.17 Jupiter masses is a huge amount of gas, these clouds should have large physical sizes and/or be relatively numerous. The discrepancy between the ISO detection and the present negative FUSE result remains a challenging issue.

Using ISO, even larger amounts of H_2 have been reported[1] for other similar, albeit younger, circumstellar disks. Again the nature and the geometrical distribution of this H_2 remain to be determined. The present result shows that, in the circumstellar disks, dust is not a good indicator of the H_2 distribution; it also shows that CO may not generally be as depleted in the disks as may be concluded simply from the observed ratio of CO and H_2 emission. On the contrary, CO could be over-abundant compared to the standard CO/H_2 ratio; this provides a clue to the evaporation activity related to large-scale motions of the remnant planetesimals being cleared from the young planetary disk. □

Received 14 March; accepted 12 June 2001.

1. Thi, W. F. *et al.* Substantial reservoirs of molecular hydrogen in the debris disks around young stars. *Nature* **409,** 60–63 (2001).
2. Vidal-Madjar, A., Lecavelier des Etangs, A. & Ferlet, R. Beta Pictoris, a young planetary system? A review. *Planet. Space Sci.* **46,** 629–648 (1998).
3. Backman, D. E. & Paresce, F. Main-sequence stars with circumstellar solid material—The Vega phenomenon. *Protostars and Planets III* (eds Levy, E. H. & Lunine, J. I.) 1253–1304 (Univ. Arizona Press, 1993).
4. Lecavelier des Etangs, A., Vidal-Madjar, A. & Ferlet, R. Dust distribution in disks supplied by small bodies: is the Beta Pictoris disk a gigantic multi-cometary tail? *Astron. Astrophys.* **307,** 542–550 (1996).
5. Hobbs, L. M., Vidal-Madjar, A., Ferlet, R., Albert, C. E. & Gry, C. The gaseous component of the disk around Beta Pictoris. *Astrophys. J.* **293,** L29–L33 (1985).
6. Vidal-Madjar, A., Ferlet, R., Hobbs, L. M., Gry, C. & Albert, C. E. The circumstellar gas cloud around Beta Pictoris. II. *Astron. Astrophys.* **167,** 325–332 (1986).
7. Lagrange, A.-M. *et al.* The Beta Pictoris circumstellar disk. XXIV. Clues to the origin of the stable gas. *Astron. Astrophys.* **330,** 1091–1108 (1998).
8. Roberge, A. *et al.* High-resolution Hubble Space Telescope STIS spectra of CI and CO in the Beta Pictoris circumstellar disk. *Astrophys. J.* **538,** 904–910 (2000).
9. Vidal-Madjar, A. *et al.* HST-GHRS observations of Beta Pictoris: additional evidence for infalling comets. *Astron. Astrophys.* **290,** 245–258 (1994).
10. Jolly, A. *et al.* HST - GHRS observations of CO and CI in the Beta Pictoris circumstellar disk. *Astron. Astrophys.* **329,** 1028–1034 (1998).
11. van Dishoeck, E. F. & Black, J. H. The photodissociation and chemistry of interstellar CO. *Astrophys. J.* **334,** 771–802 (1988).
12. Barrado y Navascués, D., Stauffer, J. R., Song, I. & Caillault, J.-P. The age of Beta Pictoris. *Astrophys. J.* **520,** L123–L126 (1999).
13. Ferlet, R., Vidal-Madjar, A. & Hobbs, L. M. The Beta Pictoris circumstellar disk. V- Time variations of the CA II-K line. *Astron. Astrophys.* **185,** 267–270 (1987).
14. Beust, H., Vidal-Madjar, A., Ferlet, R. & Lagrange-Henri, A. M. The Beta Pictoris circumstellar disk. X-Numerical simulations of infalling evaporating bodies. *Astron. Astrophys.* **236,** 202–216 (1990).
15. Carruthers, G. R. Rocket observation of interstellar molecular hydrogen. *Astrophys. J.* **161,** L81–L85 (1970).
16. Spitzer, L. *et al.* Spectrophotometric results from the Copernicus satellite. IV. Molecular hydrogen in interstellar space. *Astrophys. J.* **181,** L116–L121 (1973).
17. Shull, J. M. & Beckwith, S. Interstellar molecular hydrogen. *Annu. Rev. Astron. Astrophys.* **20,** 163–190 (1982).
18. Moos, H. W. *et al.* Overview of the Far Ultraviolet Spectroscopic Explorer Mission. *Astrophys. J.* **538,** L1–L6 (2000).
19. Deleuil, M. *et al.* Is Beta Pictoris an active star? *Astrophys. J.* (in the press).
20. Roberge, A. *et al.* FUSE and HST STIS observations of hot and cold gas in the AB Aurigae system. *Astrophys. J.* **551,** L97–L100 (2001).
21. Magnani, L., Onello, J. S., Adams, N. G., Hartmann, D. & Thaddeus, P. The variation of the CO to H_2 conversion factor in two translucent clouds. *Astrophys. J.* **504,** 290–299 (1998).
22. Kamp, I. & Bertoldi, F. CO in the circumstellar disks of Vega and Beta Pictoris. *Astron. Astrophys.* **353,** 276–286 (2000).
23. Lecavelier des Etangs, A. Circumstellar disks and outer planet formation. *Planets Outside the Solar System: Theory and Observations* (eds Mariotti, J.-M. & Alloin, D.) 95–103 (Kluwer Academic, Dordrecht/Boston, 1999).
24. Liseau, R. & Artymowicz, P. High sensitivity search for molecular gas in the Beta Pic disk. On the low gas-to-dust mass ratio of the circumstellar disk around Beta Pictoris. *Astron. Astrophys.* **334,** 935–942 (1998).

Acknowledgements

We thank Gopal-Krishna, G. Pineau des Forêts and S. Cabrit for discussions, and R. Kurucz for providing a model of the β Pic stellar atmosphere. The work at Johns Hopkins University was supported by NASA; the work at the Institut d'Astrophysique de Paris and at LAM was supported by CNES. The work reported here is based on data obtained by the NASA-CNES-CSA FUSE mission, operated by the Johns Hopkins University.

Correspondence and requests for materials should be addressed to A.L.d.E. (e-mail: lecaveli@iap.fr).

Origin of the Moon in a giant impact near the end of the Earth's formation

Robin M. Canup* & Erik Asphaug†

* *Department of Space Studies, Southwest Research Institute, 1050 Walnut Street, Suite 426, Boulder, Colorado 80302, USA*
† *Department of Earth Sciences, University of California, Santa Cruz, California 95064, USA*

The Moon is generally believed to have formed from debris ejected by a large off-centre collision with the early Earth[1,2]. The impact orientation and size are constrained by the angular momentum contained in both the Earth's spin and the Moon's orbit, a quantity that has been nearly conserved over the past 4.5 billion years. Simulations of potential moon-forming impacts now achieve resolutions sufficient to study the production of bound debris. However, identifying impacts capable of yielding the Earth–Moon system has proved difficult[3–6]. Previous works[4,5] found that forming the Moon with an appropriate impact angular momentum required the impact to occur when the Earth was only about half formed, a more restrictive and problematic model than that originally envisaged. Here we report a class of impacts that yield an iron-poor Moon, as well as the current masses and angular momentum of the Earth–Moon system. This class of impacts involves a smaller—and thus more likely—object than previously considered viable, and suggests that the Moon formed near the very end of Earth's accumulation.

The strength of the impact hypothesis over alternative models rests on its ability to account for (1) the initial ~5-hour terrestrial day implied by the Earth–Moon system angular momentum ($L_{\mathrm{E-M}} = 3.5 \times 10^{41}\ \mathrm{g\,cm^2\,s^{-1}}$); and (2) the ejection of sufficient iron-depleted material into orbit to yield the Moon, which has an unusually small metallic core comprising $\lesssim$3% of its mass[7]. Many works[3–5,8–12] have modelled potential moon-forming impacts, most using a method known as smooth particle hydrodynamics, or SPH[13]. In SPH, objects are evolved in time by estimating their state and dynamical variables at discrete points that are smoothed over spherical overlapping kernel functions. This lagrangian technique requires no underlying grid, and is well suited to intensely deforming systems evolving within mostly empty space.

Recent SPH simulations[4,5] identify two classes of impacts capable of placing sufficient mass into orbit to yield the Moon, but neither is entirely satisfactory. The first involves impacts with angular momentum, L_{imp}, much greater than $L_{\mathrm{E-M}}$, typically by a factor of 2. A significant dynamical event, for example another giant impact, would then be required to decrease the Earth–Moon system angular momentum by such a large amount. The second involves impacts with $L_{\mathrm{imp}} \approx L_{\mathrm{E-M}}$, but with a total mass (impactor plus target) of only $M_{\mathrm{T}} \approx 0.65M_{\oplus}$, where $M_{\oplus}$ is the mass of the Earth (5.98×10^{27} g). In this 'early Earth' scenario, the Earth is only partially accreted when the Moon forms and must subsequently gain about $0.35M_{\oplus}$, with the later growth involving sufficiently small and numerous impacts that the system angular momentum is not substantially altered[5]. If, during this period, the Moon also accumulated even an approximately proportionate amount of material, it would have gained excessive amounts of iron. The ratio of impact rate onto the Moon versus that with the Earth is $N_1 = f_{\mathrm{M}}R_{\mathrm{M}}^2/f_{\oplus}R_{\oplus}^2$, where $f_{\mathrm{M}}/f_{\oplus}$ is the ratio of the gravitational focusing factor of the Moon to that of the Earth, and R_{M} and $R_{\oplus}$ are the lunar and terrestrial radii. Reasonable values of impactor velocity yield[14] $0.03 < N_1 < 0.074$; assuming an impacting population with a terrestrial abundance of iron implies that the Earth could accrete only about $0.05M_{\oplus}$ before impacts with the Moon delivered an amount of iron equal to the upper limit on the mass of the lunar core.

It has recently been shown[6] that simulations with a fixed ratio $\gamma = M_{\mathrm{imp}}/M_{\mathrm{T}}$ of the impactor-to-total mass yield a maximum

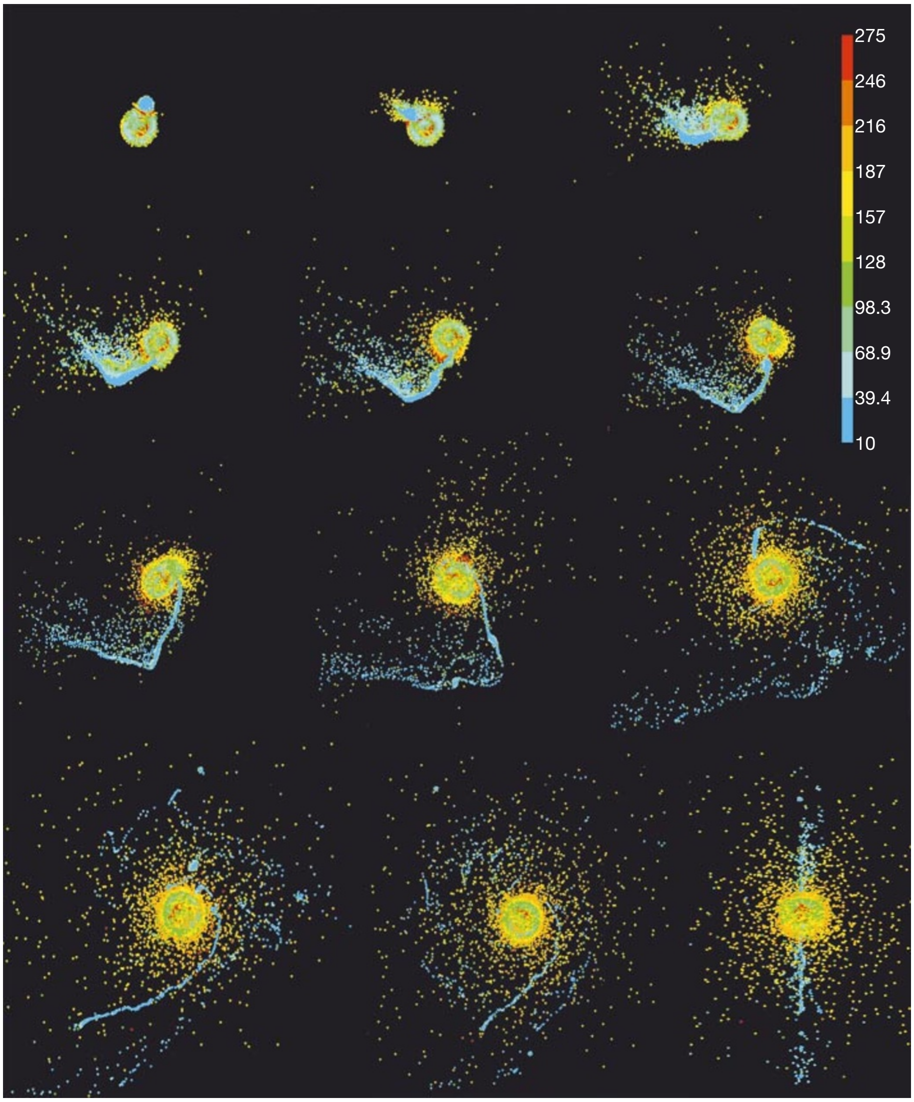

Figure 1 Time series of a Moon-forming impact simulation. Results are shown looking down onto the plane of the impact at times $t = 0.3$, 0.7, 1.4, 1.9, 3, 3.9, 5, 7.1, 11.6, 17 and 23 hours (from left to right); the last frame is $t = 23$ hours viewed on-edge. Colour scales with internal energy (shown on the colour bar in units of 6.67×10^8 erg g^{-1}), so that blue and dark green represents condensed matter, and red particles signify either the expanded phase or a hot, high-pressure condensed phase; pressures at intermediate energies are computed by an interpolation between the Tillotson[15] condensed and expanded phases. We form initial impactors and targets in hydrostatic equilibrium by pre-colliding smaller bodies together at zero incidence, resulting in realistically evolved internal energies, stratified densities (basalt mantle + iron core) and consistent pressures. Each particle's internal energy is evolved due to the effects of expansion/compression and shock dissipation, with the latter represented by artificial viscosity terms that are linear and quadratic in the velocity divergence of converging particles; effects of mechanical strength and radiative transfer are ignored. The momentum of each particle is evolved due to pressure, viscous dissipation and gravity. Gravity is computed using a binary tree algorithm, reducing the N^2 calculation of particle–particle attractions into an $N\log N$ calculation[25]. We use a beta spine kernel to define the spatial distribution of material represented by each SPH particle. The scale of each particle, h, is automatically adjusted to cause overlap with a minimum of 40 other particles, ensuring a 'smoothed' distribution of material even in low-density regions. The code is explicit, requiring a Courant-limited timestep $\Delta t < (c/h)$ where c is the sound speed. For a full description of the technique, see ref. 26, from whose efforts our present algorithm derives.

orbiting mass when the impact parameter $b \approx 0.8$ ($b = L_{\rm imp}/L_{\rm graz} = 0$ and 1 for head-on and grazing collisions, and no collision occurs for $b > 1$). This result is independent of the total colliding mass $M_{\rm T}$. Accordingly, the maximum yield for an $L_{\rm imp} \approx L_{\rm E-M}$ and $M_{\rm T} \approx M_{\oplus}$ impact should be achieved when $b \approx L_{\rm E-M}/L_{\rm graz} \approx 0.8$, with the angular momentum of a grazing impact, $L_{\rm graz}$, given by (assuming an impact velocity, $v_{\rm imp}$, equal to the mutual escape velocity of the colliding bodies, $v_{\rm esc}$):

$$L_{\rm graz} = [3/(4\pi\rho)]^{1/6}\sqrt{2Gf(\gamma)M_{\rm T}^{5/3}} \tag{1}$$

where G is the gravitational constant, ρ is the average target/impactor density, and $f(\gamma) \equiv \gamma(1-\gamma)[\gamma^{1/3} + (1-\gamma)^{1/3}]^{1/2}$. Setting $L_{\rm E-M}/L_{\rm graz} = 0.8$ and $M_{\rm T} = M_{\oplus}$ yields a predicted optimal impactor-to-total mass ratio of $\gamma \approx 0.1$.

Colliding objects with $\gamma < 0.12$ had been ruled out as lunar-forming candidates in early low-resolution studies[9], because they appeared to produce overly iron-rich disks. However, for those simulations with $N = 3{,}000$ particles, a single iron particle contained a mass comparable to the upper limit on the lunar core. We now use increased resolution to revisit the smaller-impactor scenario, with ejected debris described by 10^2–10^3 particles. With higher resolution, (1) the shock wave is better resolved, and it is the shock and its release that are responsible for the flow field and the expansion of vapour at the impactor/target boundary; (2) errors implicit in sparse particles are reduced, as SPH only has meaning as an interpolation technique over sets of overlapping particles; and (3) the granularity of the gravitational potential of orbiting debris is lessened. Such issues were recognized previously, but $\gamma < 0.12$ impacts have not been re-examined until now.

Figure 1 shows a time series of a simulation with $N = 30{,}000$ particles (run 24; see Table 1), in which the mass ratio $\gamma = 0.11$. At the end of this simulation, the planet contains $0.99M_{\oplus}$ and the mass of orbiting debris is $M_{\rm D} = 1.68M_{\rm M}$ (where $M_{\rm M} = 0.012M_{\oplus}$ is a lunar mass). Of the orbiting mass, 2.0% is iron, with 80% of this iron located within the Earth's Roche limit (the distance interior to which a strengthless, self-gravitating object would be torn apart by Earth's tidal forces), where $a_{\rm Roche} = 2.9R_{\oplus}$ for lunar and terrestrial densities. The orbiting material consists of a cooler component that forms a flattened equatorial disk, and a hot, pressure-supported component that comprises a vertically thick cloud enshrouding the planet.

Our simulations (like those of refs 8–10) rely upon the Tillotson[15] equation of state (EOS) to calculate pressure. The Tillotson EOS is a relatively simple EOS developed for strong shocks in metals and geologic media. Direct comparisons[16] between simulations using the code employed here and that of Cameron[4] utilizing a more sophisticated EOS, known as ANEOS[10], show general similarities in the predicted amount of mass and angular momentum placed into orbit, with the latter consistent to ~10%. However, these comparisons showed significant differences in the implied physical state of the orbiting material. Unlike the Tillotson EOS, ANEOS handles mixed phases; however, in its current rendition ANEOS treats all vapour as monatomic species[17]. The entropy required for vaporization of molecular species such as mantle rock is therefore greatly overestimated by ANEOS, and a remedy to this is being undertaken by Melosh[18]. This EOS problem or a related error may contribute to the perplexing near-zero temperatures in the mantle and core of the final protoearth in Cameron's recent simulations[4]. For now, we

Table 1 Parameters and results of impact simulations

Run	$M_{\rm T}/M_{\oplus}$	γ	$L_{\rm imp}/L_{\rm graz}$	$L_{\rm imp}/L_{\rm E-M}$	$L_{\rm D}/L_{\rm E-M}$	$L_{\rm final}/L_{\rm E-M}$	$M_{\rm esc}/M_{\rm M}$	$M_{\rm Fe}/M_{\rm D}$	$M_{\rm D}/M_{\rm M}$	$M_{\rm D}/M_{\rm M} > a_{\rm Roche}$	$M/M_{\rm M}$
1	1.018	0.08	0.98	1.07	0.27	0.80	1.11	0.32	1.50	0.86	1.13
3	1.018	0.09	0.88	1.07	0.29	1.00	0.48	0.05	1.50	0.82	1.30
9	1.018	0.09	0.90	1.10	0.25	0.90	0.94	0.12	1.37	0.82	1.04
17	1.018	0.09	0.94	1.15	0.30	0.92	0.98	0.16	1.51	1.04	1.40
18	1.018	0.09	0.98	1.20	0.30	0.88	1.28	0.24	1.62	1.02	1.29
54	**0.980**	**0.097**	**0.84**	**1.04**	**0.30**	**0.97**	**0.48**	**0.01**	**1.32**	**0.92**	**1.32**
53	0.980	0.097	0.90	1.12	0.24	0.93	0.89	0.07	1.31	0.74	1.02
2	1.019	0.10	0.80	1.07	0.22	1.00	0.53	0.01	1.18	0.66	0.96
14	**1.109**	**0.10**	**0.82**	**1.10**	**0.28**	**1.03**	**0.48**	**0.01**	**1.40**	**0.78**	**1.32**
23	**1.019**	**0.10**	**0.84**	**1.12**	**0.30**	**1.05**	**0.50**	<**0.01**	**1.35**	**0.87**	**1.35**
8	1.019	0.10	0.85	1.15	0.28	1.07	0.52	0.04	1.32	0.76	1.30
16	1.019	0.10	0.87	1.17	0.23	0.98	0.91	0.04	1.36	0.50	0.84
15	1.019	0.10	0.89	1.20	0.27	1.00	0.98	0.05	1.50	0.75	1.03
5	1.019	0.107	0.75	1.07	0.12	0.99	0.61	0.02	0.78	0.20	0.36
21	1.019	0.107	0.77	1.10	0.19	1.03	0.56	0.02	1.09	0.51	0.74
12	**1.019**	**0.107**	**0.80**	**1.15**	**0.26**	**1.07**	**0.55**	**0.01**	**1.27**	**0.78**	**1.27**
[c]59	**0.990**	**0.107**	**0.82**	**1.13**	**0.31**	**1.06**	**0.45**	**0.01**	**1.59**	**0.97**	**1.49**
6	**1.019**	**0.107**	**0.82**	**1.18**	**0.34**	**1.10**	**0.55**	**0.01**	**1.69**	**1.16**	**1.69**
[c]31	**1.012**	**0.107**	**0.82**	**1.16**	**0.30**	**1.07**	**0.67**	**0.01**	**1.52**	**0.73**	**1.33**
22	**1.019**	**0.107**	**0.84**	**1.20**	**0.32**	**1.12**	**0.54**	**0.03**	**1.47**	**1.04**	**1.47**
[c]60	0.990	0.107	0.90	1.23	0.33	1.04	0.88	0.09	1.82	1.00	1.38
11	1.019	0.107	0.90	1.29	0.31	1.08	1.00	0.05	1.71	0.96	1.29
4	1.019	0.11	0.73	1.07	0.09	0.99	0.59	<0.01	0.66	0.06	0.25
10	1.019	0.11	0.75	1.10	0.14	1.02	0.59	0.01	0.92	0.22	0.42
19	**1.019**	**0.11**	**0.78**	**1.15**	**0.24**	**1.07**	**0.56**	**0.01**	**1.22**	**0.70**	**1.04**
25	**0.980**	**0.11**	**0.80**	**1.11**	**0.28**	**1.03**	**0.65**	<**0.01**	**1.31**	**0.89**	**1.31**
[a]36	**1.019**	**0.11**	**0.82**	**1.20**	**0.22**	**1.10**	**0.76**	<**0.01**	**1.23**	**0.57**	**1.00**
[b]35	**1.019**	**0.11**	**0.82**	**1.20**	**0.36**	**1.11**	**0.71**	<**0.01**	**1.68**	**1.26**	**1.68**
20	**1.019**	**0.11**	**0.82**	**1.20**	**0.33**	**1.12**	**0.51**	<**0.01**	**1.60**	**1.12**	**1.58**
[c]24	**1.019**	**0.11**	**0.82**	**1.20**	**0.34**	**1.12**	**0.50**	**0.02**	**1.68**	**0.97**	**1.48**
[d]34	**1.017**	**0.11**	**0.82**	**1.20**	**0.31**	**1.12**	**0.64**	**0.02**	**1.50**	**0.81**	**1.50**
26	**0.980**	**0.11**	**0.82**	**1.13**	**0.34**	**1.05**	**0.64**	**0.01**	**1.59**	**1.19**	**1.59**
27	**0.980**	**0.11**	**0.84**	**1.15**	**0.34**	**1.07**	**0.58**	**0.01**	**1.65**	**1.27**	**1.65**
28	0.970	0.115	0.78	1.10	0.19	1.01	0.74	0.01	1.09	0.54	0.78
29	**0.970**	**0.115**	**0.80**	**1.13**	**0.31**	**1.05**	**0.66**	<**0.01**	**1.50**	**1.01**	**1.50**
30	**0.970**	**0.115**	**0.82**	**1.16**	**0.36**	**1.08**	**0.63**	**0.01**	**1.75**	**1.19**	**1.75**

At the end of each run, we classify particles as escaping (positive kinetic + potential energies), orbiting, or within the planet. A particle is considered to be orbiting if its total energy is negative, and the z-component of its angular momentum exceeds that of a circular orbit at the surface of the planet. We use an iterative analytic method[6,16] to solve for the mass and radius of the final planet in order to maintain consistency across different simulations. First, an estimate of the fraction of mass contained in the planet is used to calculate the amount of escaping and bound debris; this yields an updated value for the planet's mass and radius, assuming a terrestrial bulk density. Results shown are at approximately 24 hours post-impact; for resolutions used here, numerically induced spreading in the disk[24] should be minimal on this timescale. $M_{\rm D}$ and $L_{\rm D}$ are the mass and angular momentum in orbiting debris; $M_{\rm D}/M_{\rm M} > a_{\rm Roche}$ is the orbiting mass in lunar masses that has an equivalent orbit exterior to $a_{\rm Roche}$. $M_{\rm Fe}$ is the mass of orbiting iron, and $L_{\rm final}$ is $L_{\rm imp}$ minus angular momentum of escaping debris. The nominal resolution is $N = 2 \times 10^4$ particles; runs with $N = 3 \times 10^3$, 1×10^4, 3×10^4 and 6×10^4 particles are indicated with a, b, c and d superscripts, respectively. In all cases $v_{\rm imp} = v_{\rm esc}$, with no pre-impact spin. The final column shows the predicted mass of the moon in lunar masses ($M/M_{\rm M}$) that would result (see text). Boldface indicates cases where $M/M_{\rm M} \geq 1$ and $M_{\rm Fe}/M_{\rm D} \leq 0.03$.

consider the Tillotson EOS to be more robust. Although it cannot reliably predict melt fraction, it renders shock compression and release quite well and these, as well as gravitational torques, are of primary importance in mobilising the ejected matter into orbit.

The 36 simulations listed in Table 1 were parameterized so that the resulting planet-debris system had a mass within 5% of $M_{\mathrm{E\text{–}M}}$ ($M_{\mathrm{E\text{–}M}} \equiv M_\oplus + M_{\mathrm{M}} = 1.012M_\oplus$), and a final angular momentum within about 10% of $L_{\mathrm{E\text{–}M}}$. In 4.5 billion years, a system decrease of less than $0.1L_{\mathrm{E\text{–}M}}$ would occur[6] owing to direct solar tides raised on the Earth if we assume a terrestrial tidal dissipation factor, Q, larger than $Q \approx 5$; currently, $Q \approx 12$.

Typically, the majority of orbiting debris has an equivalent circular orbit outside the Roche limit; none of our simulations produced massive disks located entirely within a_{Roche}. Most of the orbiting material originates from the impacting object rather than the target (the Earth), as seen earlier[3–4,8–11]. For the boldface cases in Table 1, the fraction of orbiting mass originating from the impactor, $M_{\mathrm{i}}/M_{\mathrm{D}}$, ranges from 0.6 to 0.74; for material with angular momentum sufficient to orbit exterior to a_{Roche}, this fraction is higher, with $M_{\mathrm{i}}(>a_{\mathrm{Roche}})/M_{\mathrm{D}}(>a_{\mathrm{Roche}}) = 0.72$ to 0.88. This implies that the Moon will accrete from primarily impactor-originating material, with a possible target contribution of up to tens of per cent by mass. However the relative amount of ejecta from the impactor versus target may be affected by the EOS treatment of vaporization[16].

Larger impactors ($\gamma > 0.115$) can produce massive disks, but yield an Earth–Moon system with too much angular momentum. For a fixed L_{imp} and M_{T}, a larger γ requires a smaller impact parameter b, and under this constraint a larger γ results in less orbiting debris. Recent simulations[5] use $\gamma = 0.3$, and for this value $M_{\mathrm{D}} \leqslant 0.05M_{\mathrm{M}}$ for $L_{\mathrm{imp}} \approx L_{\mathrm{E\text{–}M}}$ and $M_{\mathrm{T}} \approx M_{\mathrm{E\text{–}M}}$. Unless a progressively smaller total colliding mass is considered (for example, for $\gamma = 0.3$, M_{T} must be reduced to about $0.65M_\oplus$; refs 4–6), it appears impossible to produce an appropriate protolunar disk for larger γ values and $L_{\mathrm{imp}} \approx L_{\mathrm{E\text{–}M}}$. On the other hand, smaller impactors ($0.08 \leqslant \gamma \leqslant 0.09$) produce disks that are too iron-rich, because their impact parameter b must be near grazing and so too much of the impactor core remains in orbit. We note however that in nearly all cases, the majority of orbiting iron is located interior to a_{Roche}, which could lead to a less iron-rich Moon than is implied by the bulk composition of the orbiting material. Still lower γ-values cannot deliver $L_{\mathrm{imp}} \geqslant L_{\mathrm{E\text{–}M}}$ for $v_{\mathrm{imp}} \approx v_{\mathrm{esc}}$, unless the planet is already spinning rapidly in the same sense as the collision.

Four simulations of the impact shown in Fig. 1 with varied resolutions predict a mean orbiting mass of $\langle M_{\mathrm{D}}\rangle = 1.62M_{\mathrm{M}} \pm 0.15$ and a mean angular momentum in orbiting material of $\langle L_{\mathrm{D}}\rangle = 0.335L_{\mathrm{E\text{–}M}} \pm 0.036$. In some of the lower-resolution runs (for example, runs 35 and 20) we find that a large intact moon forms as a direct result of the impact (also observed earlier[9,10]), whereas

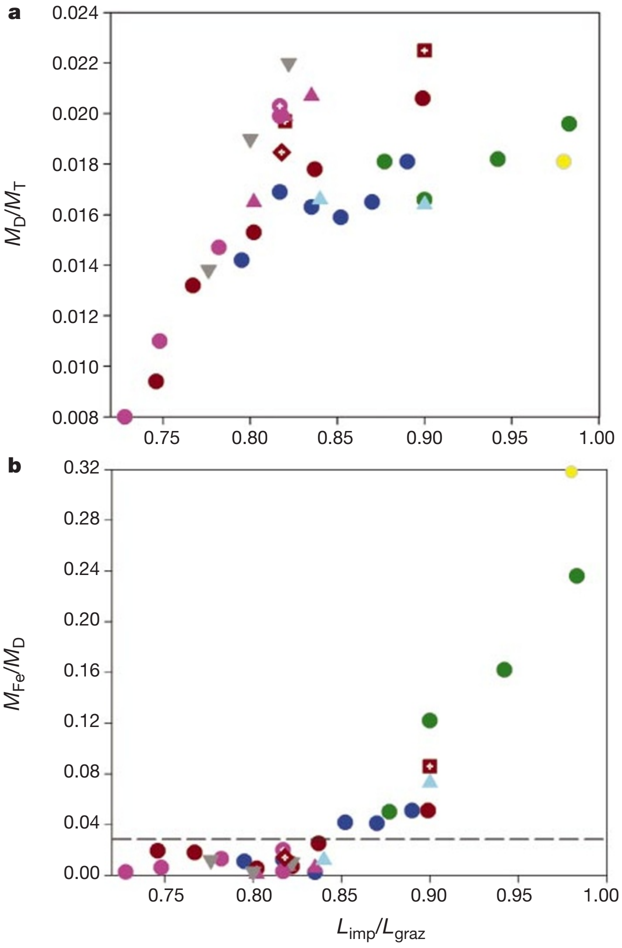

Figure 2 Scaled smooth particle hydrodynamics simulation results. **a**, The orbiting mass, M_{D}, scaled by the total colliding mass, M_{T}, as a function of $b = L_{\mathrm{imp}}/L_{\mathrm{graz}}$, where b is the impact parameter, with $b = 1$ for a grazing impact. **b**, The mass fraction of iron in the orbiting mass, $M_{\mathrm{Fe}}/M_{\mathrm{D}}$ versus $L_{\mathrm{imp}}/L_{\mathrm{graz}}$. A disk iron composition equal to the approximate mass fraction of the lunar core ($M_{\mathrm{Fe}}/M_{\mathrm{D}} = 0.03$) (ref. 7) is shown by the horizontal dashed line. Colours vary with the impactor-to-total-mass ratio, γ, with yellow, green, cyan, blue, dark red, magenta and grey corresponding respectively to $\gamma = 0.08$, 0.09, 0.097, 0.10, 0.107, 0.11 and 0.115. Symbols vary with total mass: $M_{\mathrm{T}} = 0.97M_\oplus$ (inverted-triangle), $M_{\mathrm{T}} = 0.98M_\oplus$ (triangle), $M_{\mathrm{T}} = 0.99M_\oplus$ (square), $M_{\mathrm{T}} = 1.01M_\oplus$ (diamond) and $M_{\mathrm{T}} = 1.02M_\oplus$ (circle). Simulations with $N = 30{,}000$ have a white cross-hatch within their respective symbols; all others have $N = 20{,}000$.

higher-resolution runs of the same impact (runs 24 and 34) produce a debris disk. The number of particles dictates the coarseness of the gravity potential, especially in a drawn-out bar of material. When the scale of particles is larger than the wavelength of the physical instability in the continuum those particles represent, collapse might ensue, whereas a more finely resolved system would be drawn apart by tidal shearing. This artefact of low-resolution was noticed in models[19] for the tidal disruption of comet Shoemaker–Levy 9.

Figure 2 shows scaled data from Table 1. General trends with increasing impact parameter are seen across runs with different total masses and γ values; there is also a dependence of the maximum yield on γ. For $b > 0.85$, orbiting material contains more than 3% iron by mass, with this fraction increasing progressively until a disk with a similar iron-mantle composition to that of the impactor is achieved for grazing impacts[6].

Models of protolunar disk accretion[20–22] find that a large moon forms at a characteristic distance of about $1.2a_{\rm Roche}$, with a mass that is a function of the initial disk mass and angular momentum:

$$M \approx 1.9L_{\rm D}/\sqrt{GM_{\oplus}a_{\rm Roche}} - 1.1M_{\rm D} - 1.9M_{\rm esc} \qquad (2)$$

where $M_{\rm esc}$ is the amount of escaping material during accretion. Using $M_{\rm esc} = 0.05M_{\rm D}$ (refs 21, 22), we estimate the moon mass that would result in the final column of Table 1; simulations for which this value is at least a lunar mass with $M_{\rm Fe}/M_{\rm D} \leqslant 0.03$ are shown in boldface.

The successful impacts involve an impactor-to-target mass ratio $\gamma \approx 0.1$–0.11, or an impactor with a mass of ~ 6–6.5×10^{26} g—the mass of Mars. This class of impacts represents the least restrictive impact scenario, requiring little or no dynamical modification of the Earth–Moon system after the moon-forming impact. Problems associated with a period of extended terrestrial growth subsequent to the event are avoided; in addition, the smaller impact we advocate is more likely than the 2–3 times more massive impactors postulated by recent works[4,5]; this is because in collisional populations small objects are more common than large ones (the number of objects, dN, in a mass range dm is typically proportional to $dN \propto m^{-q}dm$, with[23] $q \approx 1.5$ to 1.8). It is, in retrospect, interesting that the Mars-mass impactor that now appears to be the most promising Moon-forming candidate is essentially that originally proposed[1], a decade before the first Moon-forming impact simulations. ☐

Received 23 April; accepted 12 June 2001.

1. Cameron, A. G. W. & Ward, W. R. The origin of the Moon. *Lunar Sci.* **7,** 120–122 (1976).
2. Hartmann, W. K. & Davis, D. R. Satellite-sized planetesimals and lunar origin. *Icarus* **24,** 504–515 (1975).
3. Cameron, A. G. W. The origin of the Moon and the single impact hypothesis V. *Icarus* **126,** 126–137 (1997).
4. Cameron, A. G. W. in *Origin of the Earth and Moon* (eds Canup, R. M. & Righter, K.) 133–144 (Univ. Arizona Press, Tucson, 2000).
5. Cameron, A. G. W. From interstellar gas to the Earth–Moon system. *Meteor. Planet. Sci.* **36,** 9–22 (2001).
6. Canup, R. M., Ward, W. R. & Cameron, A. G. W. A scaling law for satellite-forming impacts. *Icarus* **150,** 288–296 (2001).
7. Hood, L. L. & Zuber, M. T. in *Origin of the Earth and Moon* (eds Canup, R. M. & Righter, K.) 397–409 (Univ. Arizona Press, Tucson, 2000).
8. Benz, W., Slattery, W. L. & Cameron, A. G. W. The origin of the Moon and the single impact hypothesis I. *Icarus* **66,** 515–535 (1986).
9. Benz, W., Slattery, W. L. & Cameron, A. G. W. The origin of the Moon and the single impact hypothesis II. *Icarus* **71,** 30–45 (1987).
10. Benz, W., Cameron, A. G. W. & Melosh, H. J. The origin of the Moon and the single impact hypothesis III. *Icarus* **81,** 113–131 (1989).
11. Cameron, A. G. W. & Benz, W. The origin of the Moon and the single impact hypothesis IV. *Icarus* **92,** 204–216 (1991).
12. Melosh, H. J. & Kipp, M. E. Giant impact theory of the Moon's origin: first 3-D hydrocode results. *Lunar Sci.* **20,** 685–686 (1989).
13. Lucy, L. B. A numerical approach to the testing of the fission hypothesis. *Astron. J.* **82,** 1013–1024 (1977).
14. Stewart, G. R. in *Origin of the Earth and Moon* (eds Canup, R. M. & Righter, K.) 217–223 (Univ. Arizona Press, Tucson, 2000).
15. Tillotson, J. H. Metallic equations of state for hypervelocity impact. Report No. GA-3216, July 18 (General Atomic, San Diego, California, 1962).
16. Canup, R. M. & Asphaug, E. Outcomes of planet-scale collisions. *Lunar Sci.* [CD-ROM] **32,** (2001).
17. Melosh, H. J. & Pierazzo, E. Impact vapor plume expansion with realistic geometry and equation of state. *Lunar Sci.* **28,** 935 (1997).
18. Melosh, H. J. A new and improved equation of state for impact computations. *Lunar Sci.* **31,** 1903 (2000).
19. Asphaug, E. & Benz, W. Size, density, and structure of comet Shoemaker-Levy 9 inferred from the physics of tidal breakup. *Icarus* **121,** 225–248 (1996).
20. Ida, S., Canup, R. M. & Stewart, G. Formation of the Moon from an impact-generated disk. *Nature* **389,** 353–357 (1997).
21. Kokubo, E., Canup, R. M. & Ida, S. in *Origin of the Earth and Moon* (eds Canup, R. M. & Righter, K.) 145–163 (Univ. Arizona Press, Tucson, 2000).
22. Kokubo, E., Makino, J. & Ida, S. Evolution of a circumterrestrial disk and formation of a single Moon. *Icarus* **148,** 419–436 (2001).
23. Greenberg, R. in *Origin and Evolution of Planetary and Satellite Atmospheres* (eds Atreya, S. K., Pollack, J. B. & Matthews, M. S.) 137–164 (Univ. Arizona Press, Tucson, 1989).
24. Nelson, A., Benz, W., Adams, F. & Arnett, D. Dynamics of circumstellar disks. *Astrophys. J.* **502,** 342–371 (1998).
25. Hernquist, L. & Katz, N. TREESPH—A unification of SPH with the hierarchical tree method. *Astrophys. J. Suppl.* **70,** 419–446 (1989).
26. Benz, W. in *Proc. NATO Adv. Res. Workshop on Numerical Modelling of Nonlinear Stellar Pulsations* (ed. Buchler, J. R.) 1–54 (Kluwer Academic, Boston, 1990).

Acknowledgements

We wish to thank Southwest Research Institute's Internal Research program for its support of development efforts for the methods utilized here, D. Terrell for securing a portion of the computational time, and P. Tamblyn for aid with some of the analysis software. A review by A. Halliday and comments provided by W. Ward, C. Agnor, D. Korycansky and R. Mihran helped to improve the paper. This research was supported by the National Science Foundation and NASA.

Correspondence and requests for materials should be addressed to R.M.C.
(e-mail: robin@boulder.swri.edu).

Sub-Planck structure in phase space and its relevance for quantum decoherence

Wojciech Hubert Zurek

Theory Division, T-6, MS B288, Los Alamos National Laboratory, Los Alamos,
New Mexico 87545, USA

Heisenberg's principle[1] states that the product of uncertainties of position and momentum should be no less than the limit set by Planck's constant, $\hbar/2$. This is usually taken to imply that phase space structures associated with sub-Planck scales ($\ll \hbar$) do not exist, or at least that they do not matter. Here I show that this common assumption is false: non-local quantum superpositions (or 'Schrödinger's cat' states) that are confined to a phase space volume characterized by the classical action A, much larger than $\hbar$, develop spotty structure on the sub-Planck scale, $a = \hbar^2/A$. Structure saturates on this scale particularly quickly in quantum versions of classically chaotic systems—such as gases that are modelled by chaotic scattering of molecules—because their exponential sensitivity to perturbations[2] causes them to be driven into non-local 'cat' states. Most importantly, these sub-Planck scales are physically significant: a determines the sensitivity of a quantum system or environment to perturbations. Therefore, this scale controls the effectiveness of decoherence and the selection of preferred pointer states by the environment[3–8]. It will also be relevant in setting limits on the sensitivity of quantum meters.

One of the characteristic features of classical chaos is the evolution of the small-scale structure in phase-space probability distributions. As a consequence of the exponential sensitivity to initial conditions, an initially regular 'patch' in phase space with a